Energy Advances

PAPER

View Article Online
View Journal | View Issue

Cite this: *Energy Adv.*, 2025, 4, 1167

Water-in-salt hydrogel electrolyte for dendrite-free Zn deposition

Varsha Joseph, [ab] Nara Kim, [ac] Sae Young Lee,[d] Reverant Crispin,[abc] Tae Hyun Park*[d] and Ziyauddin Khan *[ab]

Received 23rd June 2025,
Accepted 26th July 2025

DOI: 10.1039/d5ya00169b

rsc.li/energy-advances

Zinc metal batteries suffer from dendrite formation, hydrogen evolution, and interfacial instability. While water-in-salt electrolytes (WiSEs) suppress side reactions and hydrogels enhance interfacial stability, WiSE systems are costly and viscous, and conventional hydrogels contain excess water, promoting hydrogen evolution. To overcome these limitations, we developed a polyethylene glycol-based water-in-salt hydrogel (WiSH) electrolyte, incorporating tunable concentrations of zinc triflate ($Zn(OTf)_2$) from 1 to 4 mol kg^{-1}. The optimized 4 mol kg^{-1} formulation enabled dendrite free and corrosion-free zinc plating/stripping in symmetric Zn‖Zn cells for over 2000 hours at 1 mA cm^{-2} (1 mAh cm^{-2} area capacity), demonstrating exceptional long-term stability. The WiSH electrolyte exhibited improved mechanical strength and toughness with increasing salt concentration, attributed to stronger ionic crosslinking within the hydrogel matrix. Rheological and spectroscopic analyses confirmed the formation of a robust, densely crosslinked polymer network critical for stable and uniform Zn electrodeposition. Furthermore, a Zn–lignin full cell using the WiSH electrolyte achieved an energy density of 25 Wh kg^{-1} and 506 W kg^{-1} of specific power, highlighting its potential for energy storage systems. These results establish WiSH as a promising electrolyte platform for next-generation zinc batteries.

1. Introduction

The history of zinc-based batteries dates back to the late 18th century when Alessandro Volta first observed generation of current using zinc metal in 1796 and subsequently introduced the Voltaic pile in 1800, considered the first true chemical battery, based on zinc and copper electrodes. Since then, zinc has remained a focal material in battery research. A significant milestone was the commercial introduction of non-rechargeable zinc-air batteries in the 1970s.[1,2] However, despite decades of intense research, rechargeable zinc batteries have yet to achieve commercial viability. This lack of commercialization is not due to a lack of interest or effort; zinc continues to attract attention due to its high theoretical capacity (820 Wh kg^{-1}), natural abundance, safety, and recyclability.[3,4] Yet, the inherent challenges associated with zinc in aqueous electrolytes have remained persistent obstacles. Zinc metal is thermodynamically unstable in aqueous environments, where Zn deposition and hydrogen evolution reactions (HERs) compete at the electrode surface. The HER not only reduces efficiency but also alters the local pH at the Zn interface, creating an alkaline environment.[5] This led to the formation of $Zn(OH)_2$ ($Zn + 2H_2O \rightarrow Zn(OH)_2 + H_2$), which passivates the Zn surface, depletes active material, and disrupts ionic transport, ultimately degrading battery performance.[6] Moreover, repeated Zn plating/stripping during cycling can lead to the formation of zinc dendrites, which grow over time and may penetrate the separator, causing internal short circuits and catastrophic cell failure.[7] These interrelated issues including parasitic side reactions, passivation, and dendrite formation, collectively hinder the practical deployment of aqueous Zn-based rechargeable energy storage systems.[8] Various strategies have been explored to mitigate dendritic growth and the HER, including surface modification of the Zn anode, incorporation of electrolyte additives, and electrolyte reformulation.[9–14] However, these issues remain largely unresolved.

In 2015, the concept of water-in-salt electrolyte (WiSE) was introduced as one strategy to expand the electrochemical stability window of aqueous electrolytes.[15] The central idea was that by significantly increasing salt concentration, the activity of free water molecules could be reduced, thereby suppressing side reactions such as the HER and enabling the use of aqueous electrolytes in high-voltage battery systems. Since its conceptualization, the WiSE approach has been successfully applied to a variety of battery chemistries, including

[a] *Laboratory of Organic Electronics, Department of Science and Technology, Linköping University, SE-60174 Norrköping, Sweden. E-mail: ziyauddin.khan@liu.se*
[b] *Wallenberg Wood Science Center, Department of Science and Technology, Linköping University, SE-60174 Norrköping, Sweden*
[c] *Wallenberg initiative Materials Science for Sustainability, Department of Science and technology, Linköping University, SE-60174 Norrköping, Sweden*
[d] *Department of Organic Materials Engineering, Chungnam National University, Daejeon 34134, Republic of Korea. E-mail: taehyun.park@cnu.ac.kr*

zinc-based systems.[13,16,17] In zinc batteries, the WiSE not only mitigates the HER but also plays a crucial role in suppressing zinc dendrite formation, resulting in improved interfacial stability and enhanced cycling life. However, despite these advantages, WiSE systems face several practical limitations. These include high viscosity, low ionic conductivity,[18] leakage issues, and the requirement for thick physical separators[19] (*e.g.*, glass fiber membranes with thicknesses around 260 μm). Such factors contribute to sluggish ion transport and increased interfacial resistance, ultimately limiting the rate capability and overall electrochemical performance of the device.[6] To overcome these drawbacks, soft solid-state electrolytes such as hydrogels could be promising alternatives. Hydrogels in general offer a unique combination of mechanical flexibility, high ionic conductivity, and the ability to confine water and salt within a polymeric matrix, allowing for controlled ion transport and enhanced interface regulation.[20] However, conventional hydrogels typically contain more than 70% water, which limits their application in zinc battery systems. The high-water content promotes side reactions such as the HER which competes with zinc deposition, and results in poor performance. Since these challenges primarily stem from the presence of free water, they can be effectively mitigated using the WiSE approach. In this work, we address these limitations by integrating the principles of WiSEs with hydrogel chemistry to develop water-in-salt hydrogels (WiSHs), a hybrid system that leverages the mechanical and structural stability of hydrogels while retaining the electrochemical advantages of highly concentrated electrolytes. This synergistic design effectively overcomes mass transport barriers and interfacial instability, enabling more stable and efficient zinc deposition.[21]

Herein, we developed a polyethylene glycol polymer-based WiSH electrolyte system and investigated its effect on zinc deposition and dissolution behaviour. By systematically varying the Zn salt concentration from the salt-in-water regime 1 mol kg^{-1} (1 m) to the water-in-salt regime (4 m), we explored the impact of electrolyte composition on long-term cycling stability. Notably, at a Zn^{2+} salt concentration of 4 m, we observed stable and uniform Zn plating/stripping over 2000 hours at a current density of 1 mA cm^{-2} (corresponding capacity 1 mAh cm^{-2}) in symmetric Zn‖Zn cells. This remarkable stability may be attributed to the favourable coordination interactions between Zn^{2+} ions and the polyethylene glycol diacrylate (PEGDA) network, which likely contribute to more regulated Zn^{2+} transport at the hydrogel–Zn interface. Additionally, the reduced water activity at higher salt concentrations appears to help mitigate parasitic reactions such as dendrite growth and hydrogen evolution. Furthermore, we employed the WiSH electrolyte in a Zn–lignin full-cell configuration, where we observed promising electrochemical performance with an energy density of 25 Wh kg^{-1} and 506 W kg^{-1} of specific power. However, the long-term cycling stability of this battery still requires further optimization. Additionally, the hydrogel exhibited an ionic conductivity of 7.1×10^{-3} mS cm^{-1} even at subzero temperatures (down to −40 °C), along with enhanced mechanical stretchability at higher salt concentrations. This improvement in stretchability may be associated with the possible formation of a double-network structure, wherein ionic crosslinking complements the existing covalent framework, an effect that is often linked to increased mechanical resilience in polymeric systems.[22] Overall, this study provides valuable insights into the electrochemical behaviour of Zn in hydrogel–WiSE environments and offers a potential pathway toward the design of next-generation, dendrite-free, flexible Zn-based batteries.

2. Results and discussions

2.1. Synthesis of Zn^{2+} ion-based WiSH electrolytes

A hydrogel electrolyte was prepared using PEGDA and zinc trifluoromethanesulfonate ($Zn(OTf)_2$) (chemical structure shown in the SI, Fig. S1). The synthesis of PEGDA followed a previously reported method.[23] Subsequently, PEGDA, $Zn(OTf)_2$, and a photoinitiator 2-hydroxy-2-methylpropiophenone (HOMPP) were homogeneously dissolved in water to form the precursor solution. This solution was then poured into a polydimethylsiloxane (PDMS) mold of the desired shape (Scheme 1a). The mixture was exposed to UV irradiation to initiate the cross-linking reaction, resulting in the formation of a three-dimensional PEG-based polymeric network (Scheme 1b). Detailed synthetic procedures are provided in the Experimental section. $Zn(OTf)_2$ was added to the hydrogel electrolytes (water/PEGDA = 1 : 1) at systematically varied concentrations. The resulting samples were named "*x* m $Zn(OTf)_2$", where '*x*' indicates the molality of $Zn(OTf)_2$ within the hydrogel electrolytes where 3 m and 4 m salt concentrations are considered WiSH formulations.

2.2. Electrochemical evaluation: Zn plating/stripping tests

Prior to the detailed characterization of the hydrogel electrolytes, the Zn plating/stripping behaviour was systematically investigated using the prepared hydrogels, including WiSH formulation. Hydrogels were used as both electrolyte and separator in Zn‖Zn symmetric cells to investigate how free water content, modulated by varying $Zn(OTf)_2$ concentrations from 1 m to 4 m, affects the electrochemical reversibility of Zn plating/stripping. It would be worth mentioning here that the WiSE regime typically begins when the salt concentration exceeds ~3 m, whereas hydrogels with lower salt concentration (*e.g.*, 1 m and 2 m) based hydrogels behave more like conventional hydrogels due to their higher water content and limited ionic crosslinking. These low-salt hydrogel systems serve as effective control samples in our work. To gain insight into interfacial stability, these cells were subjected to long-term galvanostatic cycling using a systematic rate capability protocol. In this protocol, the cells were cycled at stepwise increasing current densities starting from 0.1 mA cm^{-2} (corresponding to 0.2 mA current and 0.1 mAh cm^{-2} capacity) up to 5 mA cm^{-2} (corresponding to 10 mA current and 5 mAh cm^{-2} capacity), with each current step held for 1 hour and repeated for five cycles. After this, the cells were further cycled at 1 mA cm^{-2} for extended durations to assess long-term stability. The complete dataset is provided in the SI (Fig. S2 and S3). All hydrogel electrolytes, regardless of salt concentration, successfully

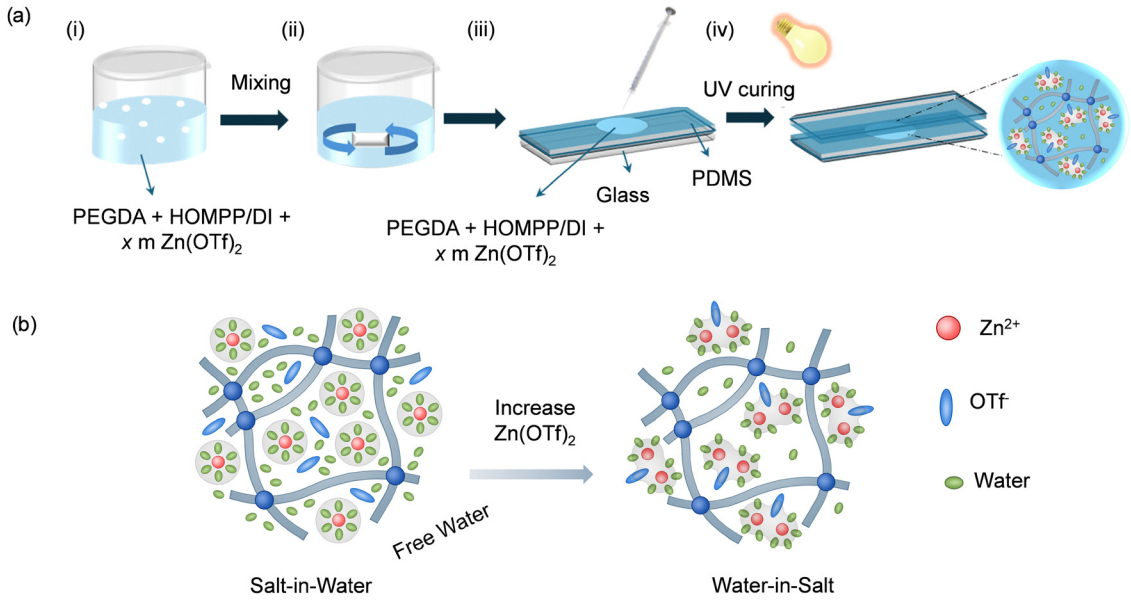

Scheme 1 Schematic illustration of (a) steps involved to prepare WiSH and (b) the 3-dimensional PEG polymeric network in the hydrogel electrolytes with different $Zn(OTf)_2$ ionic salt. Salt-in-water hydrogel electrolyte (left) and WiSH electrolyte (right).

completed the rate capability test without failure, demonstrating excellent electrochemical reversibility. Notably, cyclic stability improved with increasing salt concentration, indicating a strong dependence on the electrolyte composition. The 4 m $Zn(OTf)_2$-based WiSH electrolyte exhibited the best performance, achieving stable cycling for over 2000 hours with a consistent overpotential of ±21 mV, showing no signs of degradation or dendritic shorting throughout the test (Fig. 1a). In comparison, the lower concentration systems demonstrated more limited lifetimes, such as the1 m $Zn(OTf)_2$ hydrogel which was stable for ~300 h; 2 m $Zn(OTf)_2$ hydrogel: stable for ~450 h and 3 m $Zn(OTf)_2$ hydrogel: stable for ~1100 h. This clear trend suggests that higher salt concentration, which corresponds to lower free water content, leads to enhanced Zn interfacial stability. This is likely due to the solvation of Zn^{2+} ions, which reduces the availability of free water with increased concentration to participate in parasitic side reactions such as the HER. Suppressing the HER not only improves coulombic efficiency but also minimizes pH fluctuations at the Zn interface, which in turn reduces passivation and dendrite formation.[24] Additionally, slight increase in overpotential was observed during Zn plating/stripping in the 4 m WiSH formulation which can be attributed to its reduced ionic conductivity.[25] At high Zn^{2+} concentrations, ion–ion interactions and ion pairing limit the number of free charge carriers, while the denser hydrogel matrix increases ionic transport resistance, collectively contributing to a slight rise in overpotential despite stable long-term cycling.

To further confirm the role of water content in influencing zinc deposition behaviour, a control WiSH electrolyte was

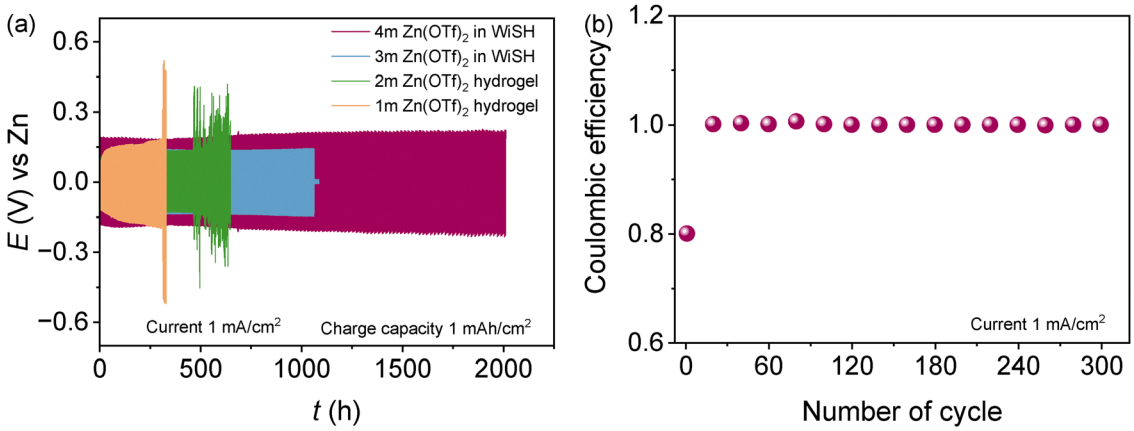

Fig. 1 (a) Comparative galvanostatic plating/stripping profiles illustrating the long-term cycling stability of Zn in hydrogel electrolytes with varying Zn^{2+} concentrations (1 m to 4 m) at 1 mA cm^{-2} current rate. Among these, the WiSH with 4 m $Zn(OTf)_2$ exhibits the most stable cycling behaviour, although a slight increase in overpotential is observed. (b) Coulombic efficiency of Zn deposition/stripping in a Ti‖Zn asymmetric cell using the optimized 4 m WiSH electrolyte, demonstrating the high reversibility of Zn plating on a non-Zn substrate.

prepared using the same 4 m $Zn(OTf)_2$ concentration, but with an increased water content during hydrogel formulation. It is important to note that, unless otherwise stated, all hydrogels in this study were prepared with a PEGDA : water ratio of 1 : 1. In this control case, however, the ratio was altered to 1 : 2, thereby introducing a higher amount of free water into the hydrogel network. Although the symmetric cell assembled with this formulation also ran for nearly 2000 hours at 1 mA cm^{-2} current, it exhibited significant overpotential fluctuations, especially at later stages (Fig. S4). This instability could be attributed to the excess free water, which likely promoted side reactions and contributed to interfacial degradation. This was further confirmed by testing Zn deposition using the Zn‖Zn symmetric cell in 4 m $Zn(OTf)_2$ solution *i.e.* WiSE where we observe cell failure at a high current of 5 mA cm^{-2} during rate capability tests (Fig. S5) suggesting the advantage of WiSH. These findings highlight a key insight of this study: achieving high Zn salt concentration in hydrogel-based WiSH electrolytes is critical for ensuring long-term dendrite-free Zn cycling and stable interfacial behaviour. This performance not only underlines the role of high salt concentration in reducing the availability of free water molecules, thereby mitigating side reactions, but also highlights the critical importance of the polymeric network, comprising both covalent and ionic cross-linking, in facilitating uniform and stable Zn plating/stripping behaviour.

To further evaluate the reversibility of Zn plating/stripping and quantify the Zn deposition efficiency, we assembled a Ti‖Zn asymmetric cell with 4 m WiSH electrolyte. The use of a titanium (Ti) working electrode serves a specific purpose: unlike symmetric Zn‖Zn cells, where both electrodes act as Zn sources, the Ti electrode has no initial zinc content, thus making it an ideal substrate to assess how efficiently Zn can be deposited and subsequently stripped. The key metric derived from this configuration is the coulombic efficiency (CE), which represents the ratio of stripped Zn to plated Zn during each cycle. In the initial cycles, we observed a relatively lower CE, likely due to side reactions such as parasitic HERs or irreversible Zn nucleation on the Ti substrate. However, with continued cycling, the CE progressively increased and approached ~100%, indicating that nearly all the electrochemically deposited Zn could be stripped back from the Ti surface up to 300 cycles at 1 mAh cm^{-2} Zn deposition capacity (Fig. 1b). This behaviour suggests that the Zn plating process gradually forms a stable and reversible Zn layer on the Ti substrate, likely facilitated by the favourable Zn^{2+} ion transport and interfacial characteristics of the WiSH electrolyte. The ability to achieve high CE over time highlights the excellent reversibility and interfacial compatibility between the WiSH electrolyte and the Ti current collector. These results further reinforce the suitability of WiSH electrolytes for high-efficiency, long-life Zn-based rechargeable batteries.

To investigate the morphology and growth behaviour of Zn during plating, Zn‖Zn symmetric cells with 4 m $Zn(OTf)_2$-based WiSH were cycled, and the plated Zn was analysed after 10 and 50 cycles. The plating/stripping experiments were carried out under identical conditions in two separate cells, and the morphology of the deposited Zn was examined using scanning electron microscopy (SEM). As a baseline comparison, the surface of pristine Zn foil was also characterized (Fig. S6), while Fig. 2a and b present the morphologies after 10 and 50 cycles, respectively. In both cycled samples, the SEM images reveal compact and dense Zn deposits with no signs of dendritic or mossy structures, indicating highly uniform Zn growth.[26] The absence of dendritic features correlates with the extended cycling stability observed in galvanostatic tests, suggesting that

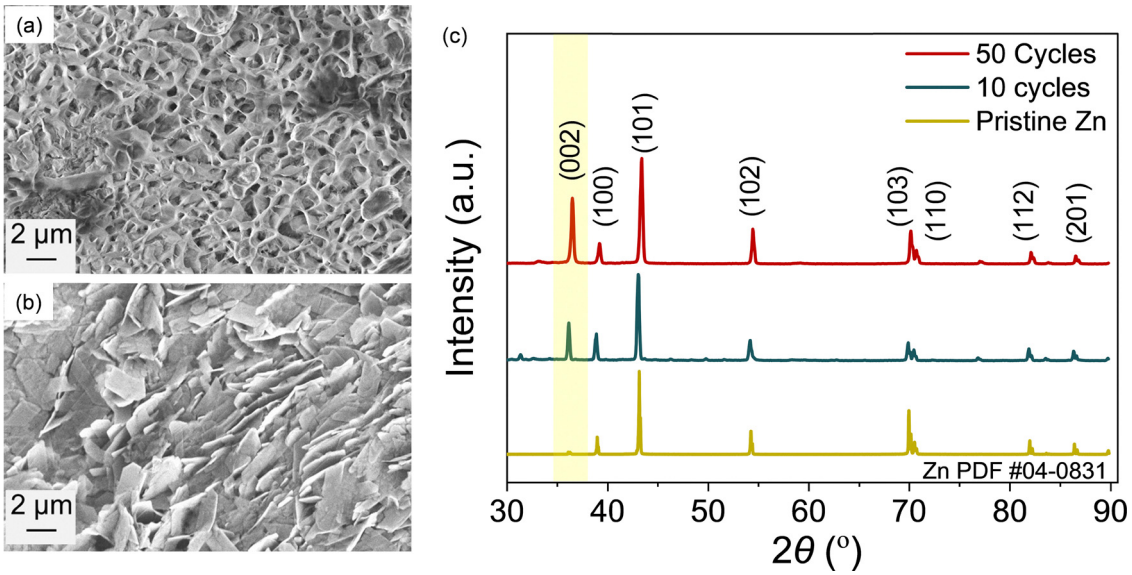

Fig. 2 SEM images of Zn electrodes after galvanostatic plating at 1 mA cm^{-2} current rate in 4 m $Zn(OTf)_2$-based WiSH: (a) after 10 cycles and (b) after 50 cycles, showing compact and uniform Zn deposition without dendritic structures (scale: 2 μm). (c) XRD patterns of pristine Zn and cycled electrodes after 10 and 50 cycles, revealing a preferential Zn growth along the (002) crystal plane during repeated deposition/stripping in symmetric Zn‖Zn cells.

the 4 m WiSH effectively promotes uniform Zn deposition and suppresses dendrite formation. To further assess the structural and phase characteristics of the deposited Zn, *ex situ* X-ray diffraction (XRD) analysis was conducted on the cycled Zn electrodes. The diffraction patterns confirm that hexagonal Zn (PDF#04-0831) remains the dominant phase after cycling, with minor zinc oxide peaks appearing around 31–32°, likely due to surface oxidation of Zn associated with the hygroscopic nature of triflate-based salts.[27,28] Importantly, a notable increase in the intensity ratio of the (002) to (100) diffraction peaks [$I_{(002)}/I_{(100)}$] was observed: increasing from 0.143 for pristine Zn to 1.09 after 10 cycles and further to 1.24 after 50 cycles. This progressive increase in the (002) texture suggests a preferential Zn deposition along the (002) crystal plane.[29] The (002) plane, which lies parallel to the substrate surface, is thermodynamically more stable and promotes lateral Zn growth. This orientation offers two key advantages: (i) it minimizes the formation of out-of-plane dendritic protrusions, reducing the risk of short-circuiting, and (ii) it presents a higher activation energy for Zn dissolution, thus improving the reversibility and structural integrity of the Zn anode during repeated cycling.[30] These crystallographic insights further validate the role of 4 m WiSH in directing favourable Zn growth behaviour, which underpins the high interfacial stability, suppressed dendrite formation, and prolonged cycling performance of Zn metal electrodes in hydrogel-based water-in-salt systems.

2.3. Physicochemical characterization of WiSH

After evaluating the electrochemical performance of various hydrogel electrolytes, we conducted detailed physicochemical characterizations of all samples. Special focus was placed on the 4 m $Zn(OTf)_2$-based WiSH, as it demonstrated the most stable and efficient Zn plating/stripping behaviour.

2.3.1. Attenuated total reflectance-Fourier transform infrared (ATR-FTIR) and Raman spectroscopy. The synthesized hydrogel electrolytes were investigated by ATR-FTIR spectroscopy to characterize the changes in the chemical bonds after UV-curing (Fig. S7). Notably, the characteristic spectral bands associated with the acrylate reactants, observed at 1636, 1620, and 1411 cm^{-1} (attributed to vibrational modes of C=C symmetric stretching, C=C asymmetric stretching, and C=CH_2– twisting, respectively) disappeared in the synthesized hydrogel electrolytes. The results indicate that UV exposure has opened the C=C double bonds in PEGDA. In other words, the ATR-FTIR analysis confirmed the formation of crosslinked PEG polymer networks within hydrogel electrolytes.

FTIR and Raman spectroscopy offer insights into material composition and component interactions *via* vibrational features and peak variations. Water molecules exhibit two distinct vibrational modes: (i) a stretching mode where the asymmetric (at 3440 cm^{-1}) and symmetric modes (at 3250 cm^{-1}) are superimposed, and (ii) a bending mode at 1650 cm^{-1}. The vibrational modes of water molecules in ATR-FTIR are significantly influenced by hydrogen bonding between free water molecules not involved in the solvation shell. Therefore, the changes in peaks indicate the dynamic nature of

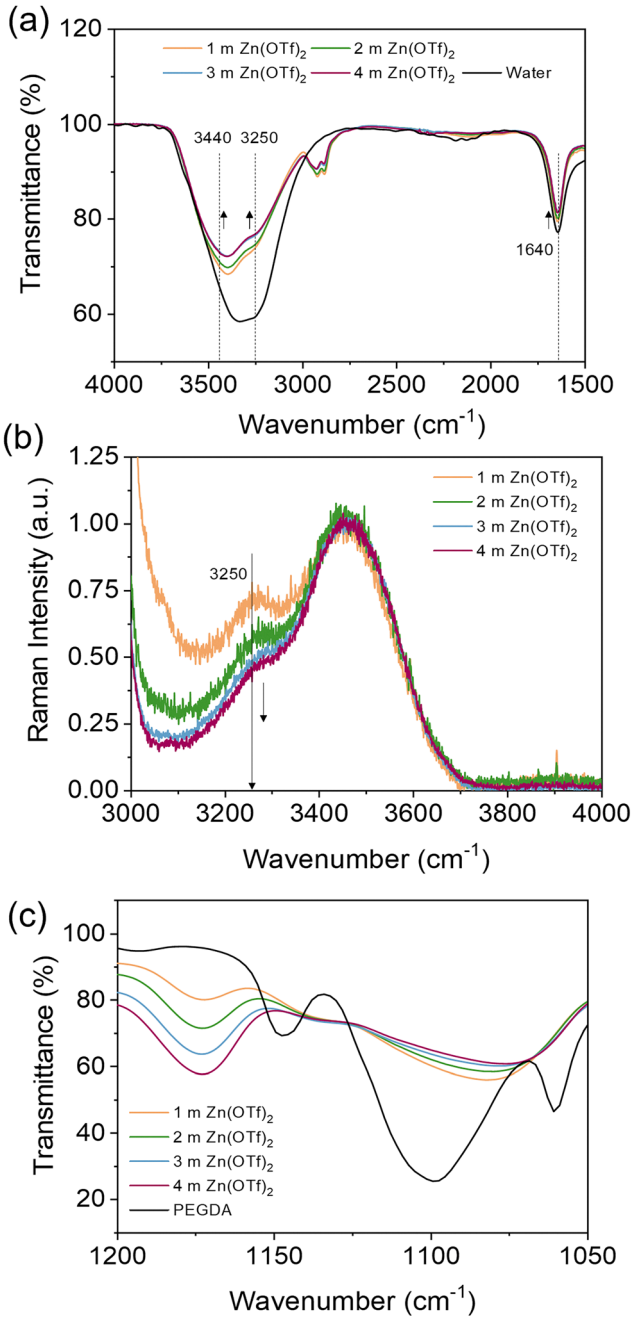

Fig. 3 (a) The ATR-FTIR transmittance curves for different hydrogel electrolytes and water. (b) Raman spectra of all hydrogel electrolytes with increasing $Zn(OTf)_2$ at room temperature. (c) The ATR-FTIR transmittance data for hydrogel electrolytes and PEGDA.

hydrogen-bonded networks between free water molecules. As shown in Fig. 3a, the addition of $Zn(OTf)_2$ ionic salt from 1 to 4 m increases the transmittance of the vibrational mode bands, indicating a decrease in absorption, for the corresponding hydrogel electrolyte. It confirms that the hydrogen bond between free water molecules in the hydrogel electrolyte is significantly suppressed because the water molecules prefer to interact with ions at high concentrations, as schematically

illustrated in Scheme 1b. Specifically, a decrease in peak intensity within the wavenumber range of 3000 to 3800 cm^{-1} related to the O–H stretching mode indicates a reduction in the presence of free water (Fig. 3a).[31] The Raman intensity at the lower wavenumber, approximately 3225 cm^{-1}, significantly decreases with $Zn(OTf)_2$ concentrations. It also indicates that the total amount of free water in the hydrogel electrolytes diminishes as the concentration of $Zn(OTf)_2$ changes from 1 m to 4 m (Fig. 3b).[32] The interaction between Zn^{2+} ions and the PEG polymer network is also observed when incorporating $Zn(OTf)_2$ ionic salt into the hydrogel electrolyte. As shown in Fig. 3c, the ATR-FTIR analysis revealed characteristic peaks (~1100 cm^{-1}) originating from the –COC– structure in the polymer backbone. The peak shifts to lower wavenumbers with increased $Zn(OTf)_2$ ionic salt. It reveals electrostatic interactions between Zn^{2+} and the oxygen atoms in the –COC– groups.

2.3.2. Ionic conductivity of WiSH. The ionic conductivity of the hydrogel electrolytes was measured using a two-electrode cell configuration *via* electrochemical impedance spectroscopy (EIS) (see the Experimental section for details). The results showed that the ionic conductivity increased with $Zn(OTf)_2$ concentration, reaching a maximum of 2.7 mS cm^{-1} for the 3 m Zn^{2+} based hydrogel (Fig. 4a and related Nyquist and Bode plots in Fig. S8). However, a further increase in salt concentration (for 4 m) led to a decline in conductivity. This behaviour can be attributed to the formation of ion pairs or aggregates at higher concentrations, which reduces the number of free charge carriers, thereby limiting ionic transport. In addition, we evaluated the temperature-dependent ionic conductivity of the 4 m WiSH electrolyte to −40 °C. Remarkably, even at such low temperatures, ion mobility was still observed (7.1 × 10^{-3} mS cm^{-1}), indicating that the hydrogel electrolyte remains partially conductive under sub-zero conditions (related Nyquist and Bode plots in Fig. S9). The ionic conductivity of the WiSH electrolyte was also compared with values reported for other hydrogel-based systems and found to be comparable, highlighting its competitive performance (Table 1).

An arrhenius plot was used to determine the activation energy for ion transport in 4 m WiSH, which was found to be 57 kJ mol^{-1}, reflecting the energy barrier associated with ionic movement through the hydrogel network below room temperature (Fig. 4b), which is comparable and even better to other reported hydrogels in similar temperature ranges (Table S1).

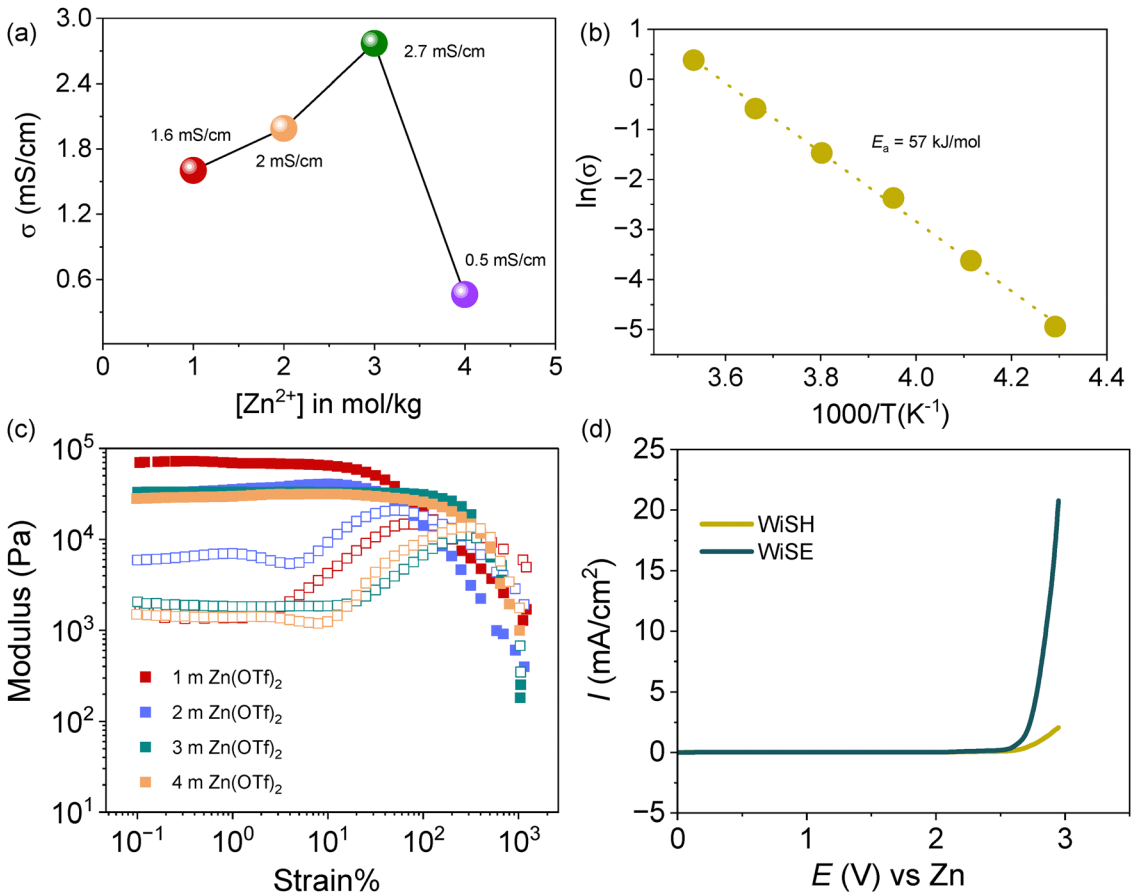

Fig. 4 (a) Ionic conductivity of hydrogels prepared at different concentrations from 1 m to 4 m. (b) Arrhenius plot of ionic conductivity experimentally measured to estimate the activation energy of the 4 m $Zn(OTf)_2$ based WiSH. (c) Variation in storage (G') and loss modulus (G'') with strain in all hydrogels. A solid rectangle represents G' modulus whereas, a hollow rectangle is associated with G'' modulus. (d) LSV of the 4 m $Zn(OTf)_2$ based WiSE and WiSH at 0.5 mV s^{-1} sweep rate using a Ti||Zn cell.

Table 1 Ionic conductivity values of reported Zn^{2+} ion-based hydrogels

Zn^{2+} concentration in hydrogel	Ionic conductivity (mS cm^{-1}) (Temp)	Zn plating/stripping cycling (h)	Current density (mA cm^{-2})	Ref.
Zwitterion hydrogel electrolyte (20 wt%)	2.6 (RT)	900	1	36
4 m $ZnCl_2$	6.26 (RT)			33
2 M $Zn(OTf)_2$	3.9 (RT)	7500	1	37
2 M $ZnSO_4$	3.93 (RT)	6000	0.5	38
1 M $Zn(TFSI)_2$	59 (RT)			39
1 m $Zn(OTF)_2$	24.8 (25 °C)	2500	1	40
2 m $ZnCl_2$	72 (26 °C)	500	5	41
2 M $ZnSO_4$	47.7 (RT)	5500	1	42
3 M $ZnSO_4$	10.4 (RT)	1000	2	43
2 M $ZnSO_4$	30.24 (RT)	1600	5	44
1 m $Zn(OTf)_2$	1.6 (RT)	375	1	Current work
2 m $Zn(OTf)_2$	2 (RT)	530	1	
3 m Zn)$OTf)_2$	2.7 (RT)	1130	1	
4 m $Zn(OTf)_2$	0.5	2000	1	
4 m $Zn(OTf)_2$	7.1×10^{-3} (−40 °C)			

The ability of the WiSH electrolyte to retain ionic conductivity at low temperatures is particularly advantageous for applications in cold environments or seasonally variable climates, where traditional aqueous electrolytes often fail due to freezing or ion transport limitations. This characteristic enhances the potential of WiSH systems for all-weather zinc-based energy storage and grid-scale applications requiring thermal resilience.[33–35]

2.3.3. Rheological measurement. The viscoelastic properties of WiSH hydrogels with varying $Zn(OTf)_2$ concentrations were investigated using a Malvern Rheometer (see the Experimental section for details). Rheological measurements included both the storage modulus (G') and the loss modulus (G''), which represent the elastic (energy-storing) and viscous (energy-dissipating) components of the hydrogel's response under oscillatory shear, respectively. G' indicates the stiffness and ability of the hydrogel to store mechanical energy, while G'' reflects the extent of energy dissipation as heat due to internal friction, corresponding to liquid-like behaviour. The rheological profiles, presented in Fig. 4c, exhibit distinct mechanical responses across different salt concentrations. At low strain, all hydrogels exhibit elastic-dominant behaviour with constant $G' > G''$, indicating intact and stable crosslinked polymer networks.[45] As the applied strain increases, G'' begins to rise, indicating the onset of energy dissipation through chain mobility and frictional losses. At a higher strain corresponding to the yield point, G' starts to decrease, suggesting breakdown of the hydrogel network. Eventually, G' and G'' intersect at the flow point ($G' = G''$), beyond which both moduli decline, reflecting the progressive disruption of the network structure. Interestingly, the 1 m $Zn(OTf)_2$ hydrogel displays the highest initial G' but yields at a lower strain (~150%), suggesting a more brittle structure with limited deformation tolerance. In contrast, hydrogels prepared with 3 m and 4 m $Zn(OTf)_2$ concentrations exhibit slightly lower initial stiffness but significantly higher yield strains where the G' starts to decrease (~350%), indicative to enhanced mechanical toughness and a more robust crosslinked network.[46,47] This trend is further supported by uniaxial tensile stress–strain data (Fig. S10), which show increasing tensile strength with salt concentration.

2.3.4. Electrochemical stability window (ESW) test for WiSH and WiSE. ESW is a critical parameter for evaluating the operational limits and durability of an electrolyte in a device with specific electrodes. To assess the ESW of the WiSH electrolyte, a Zn‖Ti cell was assembled and tested using linear sweep voltammetry (LSV) at a sweep rate of 0.5 mV s^{-1}. For comparison, a similar measurement was conducted with a conventional 4 m $Zn(OTf)_2$-based WiSE electrolyte to evaluate the impact of hydrogel formation on electrochemical stability. Both electrolytes exhibited oxidative stability beyond 2 V *vs.* Zn, indicating good resistance to oxygen evolution under moderate anodic conditions. Notably, the WiSH electrolyte demonstrated a distinct advantage: its current response remained relatively stable even up to ~3 V, in contrast to the WiSE, which showed a sharp increase in current, indicating involvement of parasitic side reactions (Fig. 4d). This improved performance in WiSH can be attributed to the presence of a crosslinked polymeric network, which effectively confines water molecules and enhances interactions between the polymer backbone and $Zn(OTf)_2$ ions. This confinement reduces water activity, suppresses side reactions, and stabilizes the electrode–electrolyte interface, thereby extending the electrochemical window. Furthermore, the effect of $Zn(OTf)_2$ concentration on the ESW of WiSH was also investigated. As shown in the SI, Fig. S11, the salt concentration did not cause a significant shift in the stability window, suggesting that the polymer matrix plays a more dominant role in determining electrochemical stability than ion concentration alone.[36,48]

To gain insight into the interfacial kinetics of the 4 m Zn salt-based WiSH, the exchange current density (i_0) was evaluated *via* Tafel polarization analysis (Fig. S12a). The Zn/WiSH interface exhibited a slightly lower exchange current density (34.5 μA cm^{-2}) compared to Zn/WiSE (37 μA cm^{-2}), indicating only a minor impact on interfacial charge-transfer kinetics despite the dense chemical crosslinking in the WiSH hydrogel. This suggests that redox reactions at the Zn interface remain relatively efficient in both systems. In addition, corrosion rates were also estimated from the Tafel parameters, revealing comparable corrosion behaviour in both electrolytes: 0.52 mmpy for WiSH and 0.56 mmpy for WiSE, further supporting that

crosslinking in WiSH does not significantly compromise electrochemical stability. To further probe the Zn/electrolyte interface, differential capacitance (C_{diff}) was measured *via* EIS at moderate frequencies (11.2 Hz and 16.6 Hz) over a range of applied potentials. Differential capacitance reflects how surface charge density changes with potential, offering insights into ion organization and mobility at the interface. For the Zn/WiSH system, the C_{diff} *vs.* potential profiles at both frequencies followed a bell shaped or U-shaped curve (a feature of electrolytes of moderate or high concentration),[49] with capacitance reaching a minimum near 0 V *vs.* Zn indicative of the potential of zero charge (Fig. S12b). Capacitance increased symmetrically on both cathodic and anodic sides, consistent with electric double layer formation due to excess ionic accumulation. Together, these findings demonstrate that WiSH provides improved ionic transport and interfacial kinetics, as reflected in its higher i_0 and C_{diff}, without a significant increase in corrosion rate.

2.3.5. Discussion. Conventionally, hydrogels are formed through hydrogen bonding interactions between polymer chains and water molecules. These non-covalent interactions cause the polymer network to swell and retain water within its three-dimensional matrix, resulting in a physically crosslinked, soft, and mechanically flexible gel structure. However, the addition of salts such as $Zn(OTf)_2$ increases system complexity by generating multiple competing interactions. Zn^{2+} cations and OTf^- anions strongly interact with water molecules and compete with the polymer for hydrogen bonding. In addition, Zn^{2+} can coordinate with electron-rich sites on the polymer chains, forming ionic or coordination bonds. These interactions act as ionic crosslinking points, enhancing the mechanical strength of the hydrogel. At low salt concentrations (*e.g.*, 1 m), hydrogen bonding between water and the polymer dominates, resulting in soft, elastic, and stretchable hydrogels. As the salt concentration increases (*e.g.*, to 3 m or 4 m), polymer–ion interactions become more prominent, creating a denser network of rigid crosslinking points. This reduces the degree of swelling and water retention, making the hydrogel tougher but less stretchable. Thus, by tuning the salt concentration, the mechanical properties of the hydrogel can be systematically controlled. In our study, higher $Zn(OTf)_2$ concentrations resulted in a mechanically robust hydrogel structure, which played a key role in suppressing dendrite formation and enhancing the stability of Zn plating/stripping.[50]

In addition to mechanical strength, hydrogels are typically composed of polymers bearing functional groups capable of coordinating with Zn^{2+} ions. These interactions can form Zn^{2+}-rich pathways that guide ion transport uniformly across the electrolyte, thereby minimizing concentration gradients of Zn^{2+} ions and suppressing their random, localized deposition that leads to dendrite formation.[36,51] Specifically, in the PEGDA-based WiSH system, Zn^{2+} ions interact with ether oxygen groups (–O–) within the polymer network, enabling controlled ion transport and promoting smooth, dendrite-free zinc deposition. Moreover, the hydrogel matrix effectively confines water molecules, thereby reducing the availability of free water and mitigating side reactions such as the HER.[36]

A natural question arises with the fact that WiSE suffers from high viscosity and cost due to its reliance on high salt concentrations: how is WiSH, which also uses concentrated Zn^{2+} salt, any better? The key lies in the role of the hydrogel matrix. In WiSE, high viscosity directly hinders ionic conductivity and slows interfacial kinetics. In contrast, when the same salt concentration is incorporated into a hydrogel framework, it does not significantly impact the bulk viscosity in the same way. Instead, the polymer network in WiSH immobilizes water and salt, forming a structured medium with localized ion channels. These channels guide Zn^{2+} ions along more uniform and controlled paths, promoting smoother and more stable Zn plating/stripping. As for cost, while the amount of salt used remains similar, WiSH provides additional value: it serves both as an electrolyte and as a separator. This multifunctionality can offset some of the material costs by simplifying cell design and improving safety and stability, making WiSH a more practical and effective alternative for zinc-based batteries.

3. Zn-lignin battery using WiSH

We fabricated a Zn-organic battery using lignin, a wood-derived material containing catechol-like electrochemically active groups.[52] Since lignin is inherently insulating, we enhanced its electrical conductivity by blending it with carbon using established methods,[17,31] resulting in an electrically conductive lignin/carbon (L/C) composite. This composite was employed as the cathode in the Zn-lignin battery using 4 m $Zn(OTf)_2$ based WiSH as electrolyte-cum-separator. To evaluate the redox activity of the lignin/carbon composite, we performed cyclic voltammetry (CV) at different scan rates ranging from 5 mV s^{-1} to 50 mV s^{-1}. At low scan rate (5 mV s^{-1}), defined redox peaks were observed, confirming the redox-active behaviour of lignin (Fig. S13). These peaks arise from the reversible redox reactions of catechol-like moieties in lignin, where hydroxyl groups (–OH) are oxidized to quinone-like structures (=O). These redox transitions are also responsible for the charge–discharge behaviour of the cell and are well-documented in lignin-based electrochemical systems.[13,31,53,54] As the scan rate increases, the redox peaks become less distinct, likely due to slow electron transfer kinetics in the L/C composite (Fig. 5a). This behaviour suggests that electrochemical reactions are kinetically limited at higher scan rates. However, the overall current increases with scan rate, which can be attributed to enhanced mass transport of ions and charge carriers at faster polarization rates. This trend is consistent with typical quasi-reversible or diffusion-controlled redox systems.

Galvanostatic charge–discharge (GCD) experiments were conducted to evaluate the specific capacity of the device. The discharge profiles exhibited non-linear behaviour across the full voltage range, which is characteristic of pseudocapacitive or faradaic processes rather than ideal capacitive behaviour and characteristic of redox-active organic electrodes. The device delivered a maximum specific capacity of 40 mAh g^{-1} at a current density of 50 mA g^{-1}, calculated based on the total

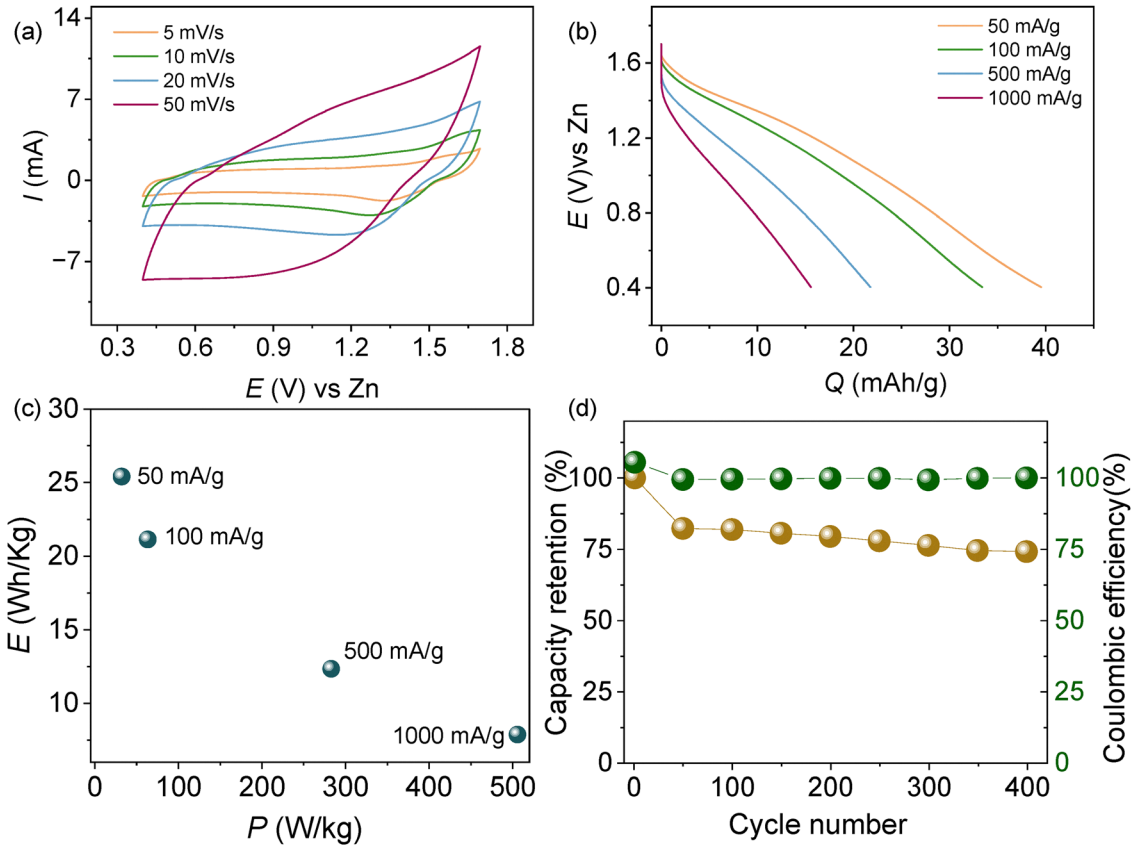

Fig. 5 (a) CV at different sweep rates ranging from 5 mV s^{-1} to 50 mV s^{-1}, (b) GCD profile at different current rates (50 mA g^{-1} to 1000 mA g^{-1}) of Zn-lignin cells. (c) Ragone plot showing maximum specific energy and maximum power of cell. (d) Capacity retention and coulombic efficiency of the Zn‖L/C battery in the WiSH at 100 mA g^{-1} of current rate.

mass of L/C electrode. As the current density increased to 1000 mA g^{-1}, the specific capacity decreased to 17 mAh g^{-1}, reflecting the typical rate-dependent behaviour due to limited ion diffusion at higher currents (Fig. 5b). The estimated maximum specific energy of the device was 25.4 Wh kg^{-1}, along with a maximum specific power output of 506 W kg^{-1}, demonstrating a promising balance between energy and power performance (Fig. 5c). Furthermore, the device exhibited good cycling stability, retaining over 75% of its initial capacity after 400 cycles at a current density of 100 mA g^{-1}, highlighting the structural and electrochemical stability of the system under prolonged operation (Fig. 5d).

4. Conclusion

In this study, we developed a WiSH electrolyte system by integrating the concepts of WiSE and hydrogels, leveraging the advantages of both. This design enables dendrite-free Zn plating/stripping while effectively addressing key challenges in conventional aqueous Zn batteries, including hydrogen evolution and corrosion. By systematically varying the $Zn(OTf)_2$ concentration, we identified the 4 m formulation as the most effective, demonstrating stable and dendrite-free Zn plating/stripping over 2000 hours at a current density of 1 mA cm^{-2}. To understand the underlying reasons for this performance, we performed comprehensive physicochemical and electrochemical characterizations using ATR-FTIR, Raman spectroscopy, EIS, LSV, and rheological analysis. These characterizations revealed that the 4 m $Zn(OTf)_2$-based WiSH forms a highly crosslinked polymeric network, resulting in enhanced mechanical integrity and reduced water activity. The rheological measurements, in particular, highlighted the superior toughness and elasticity of this hydrogel, which are essential for maintaining a stable Zn–electrolyte interface and suppressing dendritic growth during cycling. To further demonstrate the practical utility of WiSH, we assembled a Zn–lignin battery that delivered a promising maximum specific energy of 25 Wh kg^{-1} and maximum power of 506 W kg^{-1}. This proof-of-concept device highlights WiSH's potential as a safe, flexible, and durable electrolyte platform for next-generation zinc-based energy storage systems.

5. Experimental section

5.1. Materials and chemicals

Zinc trifluoromethanesulfonate (98%) was purchased from Merck. 2-Hydroxy-2-methylpropiophenone (HOMPP, 97%) was purchased from Sigma-Aldrich and used as received. Softwood kraft lignin was obtained from Backhammar.

5.2. Electrolyte preparation

HOMPP solution was prepared by dissolving 1 wt% of HOMPP in deionized (DI) water and mixing the solution using sonication. The resulting HOMPP/DI solution (the weight of HOMPP was ignored due to its relatively small amount) was then mixed with PEGDA in specific weight ratios such as 1 : 1, 1 : 2, and 1 : 3, followed by sonication until fully dissolved. An amount of x m Zn $(OTf)_2$ (x = 1, 2, 3 and 4) was then added to the solution (calculated based on the HOMPP/DI solution, ignoring the weight of HOMPP) and sonicated again until completely dissolved. The final solution was degassed to remove any bubbles.

For mold preparation, a glass slide was placed at the bottom to support the sample, followed by a rectangular polydimethylsiloxane (PDMS) layer. On top of this, a PDMS piece with a circular hole (approximately 200 μm thick and 20 mm in diameter) was placed. The solution to be cured was cast into the hole and covered with another rectangular PDMS layer (Scheme S1 in the SI). UV curing was performed using a photo exposure box equipped with a UVA lamp suitable for the HOMPP initiator. The curing process lasted for 5 minutes.

5.3. Electrode preparation and cell fabrication

The lignin/carbon (L–C) electrode was prepared *via* solvent-free mechanical ball milling of conductive carbon and kraft lignin in a planetary ball mill (TOB-XQM-4) using titanium balls. The dry weight ratio of lignin to carbon was 1 : 1. The resulting milled powder was then mixed with 10 wt% polyvinylidene fluoride (PVDF) as a binder, using *N*-methyl-2-pyrrolidone (NMP) as the solvent. The resulting slurry was coated onto graphite foil (from SGL Carbon, Germany) and dried at 60 °C for 6 hours. The wet film thickness was varied between 100 and 400 μm. After drying, the electrodes were punched into disk shapes with a diameter of 16 mm for coin cell assembly. The dry mass loading of the electrodes ranged between 2 and 3 mg cm^{-2}. Electrochemical measurements of the full cells were performed by assembling CR2032-type coin cells under ambient conditions. The L–C electrodes were used as the cathode while zinc foil (50 μm thick) served as the anode. WISH was used both as the electrolyte and as a replacement for the separator.

For device measurements, the cells were charged at various currents ranging from 50 to 1000 mA g^{-1} within a potential window of 0.4–1.7 V. The galvanostatic cycling with potential limitation (GCPL) technique was employed for galvanostatic charge–discharge (GCD) testing and for determining stored capacity. Specific energy (E) and specific power (P) were calculated using eqn (1) and (2), where m is the total mass of active materials, t is the discharge time, i is the discharge current, and V is the potential.

$$E = \frac{1}{m}\int_0^t iV\,dt \quad (1)$$

$$P = \frac{E}{t} \quad (2)$$

A Zn‖Zn symmetric cell was used to study zinc plating and stripping behaviour. Hydrogels with varying $Zn(OTf)_2$ concentrations (1–4 m) served as both electrolyte and separator. Cycling was performed at 1 mA cm^{-2}, with one-hour plating and stripping per cycle. While this configuration does not allow for direct measurement of CE due to the interchangeable nature of the zinc electrodes, it is effective for assessing the reversibility and long-term stability of zinc deposition. A Zn‖Ti cell pairs a zinc electrode with an inert Ti substrate, which serves as a stable, non-reactive current collector. Zinc is plated onto Ti during the reduction process and stripped during oxidation. Since Ti does not participate in redox reactions, this setup allows for accurate measurement of CE by comparing the amount of zinc stripped to the amount previously plated. A Tafel plot was obtained using a Zn‖Zn symmetric cell with a LSV potential range of −200 mV to 200 mV at a 0.5 mV s^{-1} sweep rate and fitted using EC lab software from Biologic which provides values for corrosion current and rates. C_{diff} was estimated using EIS at different potentials in the frequency range 1 MHz to 0.1 Hz using eqn (3) where f is frequency and Im(Z) is imaginary impedance.

$$C_{diff} = -\frac{1}{2\pi f\,\mathrm{Im}(Z)} \quad (3)$$

5.4. Electrolyte characterization

The impedance measurements were carried out using an impedance spectrometer (Alpha high-resolution dielectric analyzer, Novocontrol Technologies GmbH, Hundsangen, Germany). An AC voltage of 10 mV was applied while sweeping the frequency. The bulk ionic conductivity was calculated as $\sigma = d/(R \times A)$, where d, A, and R are the distance between the electrodes, area of cross section, and resistance, respectively. Oscillatory rheological measurements were carried out with a Malvern Rheometer (232 194) using a stainless-steel parallel plate geometry of 20 mm diameter and a gap of 0.2 mm. Amplitude tests were performed from 0.01 to 1000% strain at 1 Hz and 25-degree Celsius. ESW of the WiSH and WiSH with 4 m Zn $(OTF)_2$ was estimated using Zn metal as counter/reference electrodes and Ti as the working electrode and the tests were performed from 0 V (*vs.* Zn) to 3.0 V (*vs.* Zn) at a scan rate of 0.5 mV s^{-1}.

5.5. Attenuated total reflectance Fourier transform infrared (ATR-FTIR) and Raman spectroscopy analysis

ATR-FTIR spectroscopy analysis of the synthesized PEGDA, x m $Zn(OTf)_2$ WiSHs was recorded using an FT-IR spectrometer (Vertex 70, Bruker) under ambient conditions. Raman spectra were collected using an ND : Yag 532 nm excitation laser (LabRam Aramis, Horriba Jovin Yvon).

Conflicts of interest

There are no conflicts to declare.

Data availability

The data generated during this study are stored at a dedicated place provided by Linköping University and will be available from the authors upon reasonable request.

Chemical structure of various chemicals used, electrochemical long-term plating/stripping performance of hydrogels including WiSH and with different water content, electrochemical deposition behavior of WiSE, SEM of bare Zn foil, ATR-FTIR transmittance curves of PEGDA and hydrogel, bode and Nyquist plot for all electrolytes and WiSH at different temperatures, table comparing activation energy, mechanical strength and elasticity of hydrogels, LSV of hydrogels, Tafel plots and differential capacitance estimation of WiSH, CV of Zn-lignin battery and schematic of WiSH preparation. See DOI: https://doi.org/10.1039/d5ya00169b

Acknowledgements

The authors thank the Wallenberg Wood Science Center, the Carl Tryggers foundation and the Swedish Government Strategic Research Area in Materials Science on Functional Materials at Linköping University (Faculty Grant SFO-Mat-LiU no. 2009-00971). Z. K. acknowledges J. Gust. Richert stiftelse for project FunLig BAT (2024-00947) and the Swedish Electricity Storage and Balancing Centre (SESBC) project number MAT2023-25. The Centre is funded by the Swedish Energy Agency together with five academic and twenty-eight non-academic partners. N. K. acknowledges the Swedish Research Council (starting grant no. 2020-05218) and the Swedish Government Strategic Research Area in Materials Science on Advanced Functional Materials at Linköping University (Faculty grant SFO-Mat-LiU no. 2009-00971). This work was partially supported by the Wallenberg Initiative Materials Science for Sustainability (WISE) funded by the Knut and Alice Wallenberg Foundation. THK acknowledges support by research fund of Chungnam National University.

References

1 S. Ko, S. I. Nishimura, N. Takenaka, A. Kitada and A. Yamada, *Chem. Soc. Rev.*, 2025, **54**, 4200–4313.
2 J.-N. Liu, C.-X. Zhao, J. Wang, D. Ren, B.-Q. Li and Q. Zhang, *Energy Environ. Sci.*, 2022, **15**, 4542–4553.
3 H. Zhang, X. Liu, H. Li, I. Hasa and S. Passerini, *Angew. Chem., Int. Ed.*, 2021, **60**, 598–616.
4 S. W. D. Gourley, R. Brown, B. D. Adams and D. Higgins, *Joule*, 2023, **7**, 1415–1436.
5 Y. Liu, H. Wang, Q. Li, L. Zhou, P. Zhao and R. Holze, *Energies*, 2023, **16**, 7443.
6 Z. Khan, D. Kumar and X. Crispin, *Adv. Mater.*, 2023, **35**, 2300369.
7 Q. Li, Y. Zhao, F. Mo, D. Wang, Q. Yang, Z. Huang, G. Liang, A. Chen and C. Zhi, *EcoMat*, 2020, **2**, e12035.
8 X. Guo and G. He, *J. Mater. Chem. A*, 2023, **11**, 11987–12001.
9 Q. Wei, E. Schibli, B. Chen and S. Holdcroft, *Energy Adv.*, 2022, **1**, 606–612.
10 Q. Yang, Y. Guo, B. Yan, C. Wang, Z. Liu, Z. Huang, Y. Wang, Y. Li, H. Li, L. Song, J. Fan and C. Zhi, *Adv. Mater.*, 2020, **32**, 2001755.
11 Y. Shen, P. Fu, J. Liu, K. Sun, H. Wen, P. Liu, H. Lv, T. Gu, X. Yang and L. Chen, *Nano Res. Energy*, 2024, **3**, e9120115.
12 S. Bai, Z. Huang, G. Liang, R. Yang, D. Liu, W. Wen, X. Jin, C. Zhi and X. Wang, *Adv. Sci.*, 2024, **11**, 2304549.
13 D. Kumar, L. R. Franco, N. Abdou, R. Shu, A. Martinelli, C. M. Araujo, J. Gladisch, V. Gueskine, R. Crispin and Z. Khan, *Energy Environ. Mater.*, 2025, **8**, e12752.
14 Y. Nie, Y. Zhou, Y. Zhang, D. Sun, D. Wu, L. Ban, S. Nanda, C. Xu and H. Zhang, *Adv. Funct. Mater.*, 2025, **35**, 2418957.
15 L. Suo, O. Borodin, T. Gao, M. Olguin, J. Ho, X. Fan, C. Luo, C. Wang and K. Xu, *Science*, 2015, **350**, 938–943.
16 Y. Wang, X. Meng, J. Sun, Y. Liu and L. Hou, *Front. Chem.*, 2020, **8**, 595.
17 D. Kumar, U. Ail, Z. Wu, E. M. Björk, M. Berggren, V. Gueskine, X. Crispin and Z. Khan, *Adv. Sustainable Syst.*, 2023, **7**, 2200433.
18 I. Hwang, M. Leketas, K. Griffiths, R. Bragg, J. M. Griffin and R. A. W. Dryfe, *ChemElectroChem*, 2024, **11**, e202400099.
19 Z. Khan, D. Kumar, S. Lander, J. Phopase and R. Crispin, *EcoEnergy*, 2024, **2**, 456–465.
20 J. Lu, X. Lin, S. Wang, X. Xu, Y. Zhou, Y. Zhang, Q. Li and H. Liu, *Green Chem.*, 2023, **25**, 1635–1646.
21 W. Yi, S. Wu, Z. Zhou, X. Fang, X. Sun and J. Li, *ACS Appl. Energy Mater.*, 2023, **6**, 8838–8848.
22 H. Montazerian, E. Davoodi, A. Baidya, M. Badv, R. Haghniaz, A. Dalili, A. S. Milani, M. Hoorfar, N. Annabi, A. Khademhosseini and P. S. Weiss, *Chem. Soc. Rev.*, 2022, **51**, 9127–9173.
23 T. H. Park, B. Kim, S. Yu, Y. Park, J. W. Oh, T. Kim, N. Kim, Y. Kim, D. Zhao, Z. Ullah Khan, S. Lienemann, X. Crispin, K. Tybrandt, C. Park and S. C. Jun, *Nano Energy*, 2023, **114**, 108643.
24 M. Liu, P. Wang, W. Zhang, H. He, G. He, S. Xu, L. Yao and T. S. Miller, *Energy Storage Mater.*, 2024, **67**, 103248.
25 F. W. Fenta and R. Bouchal, *J. Mater. Chem. A*, 2024, **12**, 25035–25046.
26 H. Dai, T. Sun, J. Zhou, J. Wang, Z. Chen, G. Zhang and S. Sun, *Nat. Commun.*, 2024, **15**, 8577.
27 F. Wang, O. Borodin, T. Gao, X. Fan, W. Sun, F. Han, A. Faraone, J. A. Dura, K. Xu and C. Wang, *Nat. Mater.*, 2018, **17**, 543–549.
28 D. Li, L. Cao, T. Deng, S. Liu and C. Wang, *Angew. Chem., Int. Ed.*, 2021, **60**, 13035–13041.
29 Z. Zheng, X. Zhong, Q. Zhang, M. Zhang, L. Dai, X. Xiao, J. Xu, M. Jiao, B. Wang, H. Li, Y. Jia, R. Mao and G. Zhou, *Nat. Commun.*, 2024, **15**, 753.
30 C. Nie, G. Wang, D. Wang, M. Wang, X. Gao, Z. Bai, N. Wang, J. Yang, Z. Xing and S. Dou, *Adv. Energy Mater.*, 2023, **13**, 2300606.
31 Z. Khan, U. Ail, F. Nadia Ajjan, J. Phopase, Z. Ullah Khan, N. Kim, J. Nilsson, O. Inganäs, M. Berggren and X. Crispin, *Adv. Energy Sustainable Res.*, 2022, **3**, 2100165.
32 Z. Khan, A. Martinelli, L. R. Franco, D. Kumar, A. Idström, L. Evenäs, C. M. Araujo and X. Crispin, *Chem. Mater.*, 2023, **35**, 6382–6395.
33 Y. Wang and Y. Chen, *Electrochim. Acta*, 2021, **395**, 139178.

34 M. S. Grewal, K. Ishibashi, M. Hara, Y. Ishizaki, S. Nagano and H. Yabu, *Langmuir*, 2023, **39**, 10209–10215.
35 S. Huang, L. Hou, T. Li, Y. Jiao and P. Wu, *Adv. Mater.*, 2022, **34**, 2110140.
36 Y. Wang, Q. Li, H. Hong, S. Yang, R. Zhang, X. Wang, X. Jin, B. Xiong, S. Bai and C. Zhi, *Nat. Commun.*, 2023, **14**, 3890.
37 Y. Wang, B. Liang, D. Li, Y. Wang, C. Li, H. Cui, R. Zhang, S. Yang, Z. Chen, Q. Li, F. Mo, J. Fan and C. Zhi, *Joule*, 2025, **9**, 101944.
38 Q. He, Z. Chang, Y. Zhong, S. Chai, C. Fu, S. Liang, G. Fang and A. Pan, *ACS Energy Lett.*, 2023, **8**, 5253–5263.
39 Y. Xu, B. Lan, Y. Cheng, L. Shi, J. Sun, S. Sun and R. Wang, *J. Mater. Chem. A*, 2024, **12**, 13191–13202.
40 F. Huang, R. Wu, L. Zhang, S. Yang, J. Li, S. Zhou, Y. Guo and P. Du, *J. Power Sources*, 2025, **632**, 236343.
41 Z. Wang, R. Xue, H. Zhang, Y. Zhang, X. Tang, H. Wang, A. Shao and Y. Ma, *ACS Nano*, 2024, **18**, 7596–7609.
42 G. Li, Z. Zhao, S. Zhang, L. Sun, M. Li, J. A. Yuwono, J. Mao, J. Hao, J. Vongsvivut, L. Xing, C.-X. Zhao and Z. Guo, *Nat. Commun.*, 2023, **14**, 6526.
43 Y. Shang, R. Kokate, P. Tung, H. Zhong, E. Lizundia, F. J. Trujillo, P. Kumar and D. Kundu, *J. Mater. Chem. A*, 2025, **13**, 9555–9565.
44 J. Xu, Y. Zhu, Q. Gui, S. Sun, P. Zhao, L. Mao and T. Luo, *Small*, 2025, **21**, e2500124.
45 W. Yang and G. Yu, *J. Waterw. Port Coast. Ocean Eng.*, 2018, **144**, 05018005.
46 M. Borlaf, M. L. Picchio, G. C. Luque, M. Criado-Gonzalez, G. Guzmán-Gonzalez, D. Pérez-Antolin, G. Lingua, D. Mecerreyes and E. Ventosa, *Energy Adv.*, 2023, **2**, 1872–1881.
47 M. Kretschmer, B. Winkeljann, B. A. K. Kriebisch, J. Boekhoven and O. Lieleg, *Commun. Mater.*, 2021, **2**, 97.
48 D. Rakhman, D. Batyrbekuly, B. Myrzakhmetov, K. Zhumagali, K. Issabek, O. Sultan-Akhmetov, N. Umirov, A. Konarov and Z. Bakenov, *RSC Adv.*, 2024, **14**, 40222–40233.
49 S. Park and J. G. McDaniel, *J. Chem. Phys.*, 2024, **160**, 164709.
50 R. Zhu, H. Yang, W. Cui, L. Fadillah, T. Huang, Z. Xiong, C. Tang, D. Kowalski, S. Kitano, C. Zhu, D. R. King, T. Kurokawa, Y. Aoki and H. Habazaki, *J. Mater. Chem. A*, 2022, **10**, 3122–3133.
51 Y. Sun, L.-N. Song, X.-Y. Du, S. Liang, Y. Wang, X.-X. Wang, G.-J. Ji and J.-J. Xu, *Adv. Energy Mater.*, 2025, **15**, 2404944.
52 V. Joseph, R. Crispin and Z. Khan, *Renewable Sustainable Energy Rev.*, 2025, **223**, 116060.
53 V. C. Tran, M. Morsali, Z. Khan, R. Crispin, M. H. Sipponen and I. Engquist, *ACS Sustainable Chem. Eng.*, 2025, **13**, 9053–9062.
54 U. Ail, J. Backe, Z. U. Khan, R. Shu, J. Phopase, M. Berggren and R. Crispin, *J. Mater. Chem. A*, 2025, **13**, 2974–2986.